Energies **2013**, *6*, 3245-3262; doi:10.3390/en6073245

OPEN ACCESS

energies

ISSN 1996-1073

www.mdpi.com/journal/energies

Article

Experimental Studies on the Normal Impact of Fly Ash Particles with Planar Surfaces

Ming Dong, Sufen Li *, Jun Xie and Jian Han

School of Energy and Power Engineering, Dalian University of Technology, Dalian 116024, China; E-Mails: dongming@dlut.edu.cn (M.D.); xiejun1126@mail.dlut.edu.cn (J.X.); hanjian0822@163.com (J.H.)

* Author to whom correspondence should be addressed; E-Mail: lisuf@dlut.edu.cn; Tel./Fax: +86-411-8470-8540.

Received: 23 April 2013; in revised form: 25 June 2013 / Accepted: 27 June 2013 / Published: 3 July 2013

Abstract: This paper presents the results of a comprehensive program of experiments in which fly ash particles were impacted under controlled conditions against a flat steel surface. The overall aim of these experiments was to gain an understanding of the ash deposition process in a pulverized coal boiler system. A continuous nitrogen flow carrying fly ash particles was used to examine the effect of particle incident velocity and particle diameter (d_p) on the normal restitution coefficient, and of the particle diameter on the critical velocity. The effect of the incident normal velocity and particle diameter on the normal restitution coefficient was also examined. The results show that the normal restitution coefficient increases rapidly with increasing incident velocity when this incident velocity is less than the yield velocity, and rapidly decreases with increasing incident velocity when the incident velocity is greater than the yield velocity. The critical velocity, determined solely by the first-contact energy loss, is proportional to $d_p^{-5/6}$ and therefore becomes larger for smaller particles. For instance, in the present work, the velocity v_c of a particle with diameter of 85 μm is 0.19 m/s, which increases to 0.42 m/s for particles with a diameter of 65 μm.

Keywords: ash deposition; rebound characteristics; impaction experiments; normal restitution coefficient

---

1. Introduction

During coal combustion, ash deposition is defined as the accumulation of fly ash particles on the heat exchange surface of a boiler. Ash deposition is one of the important challenges of coal combustion [1]. If not removed, deposits may reduce the boiler thermal performance, and in severe cases, completely block flue gas channels and therefore subsequently cause unscheduled boiler shutdowns. Ash deposition may also cause severe corrosion of heat transfer surface [2].

Ash deposition characteristics are known to be influenced by coal type, reaction atmosphere, particle temperature, surface temperature of the heat exchanger, material of its surface, flow dynamics and so forth. A number of reviews relating to ash deposition characteristics have already been published. For instance, Srinivasachar *et al.* [3,4] have studied formation of the ash intermediates, which consist of gases, liquids and solids. Raask [5] elucidated deposit initiation, and Walsh *et al.* [6,7] studied deposit characteristics and growth. Beer *et al.* [8] tried to model ash behaviors. Benson *et al.* [9] summarized the behavior of ash formation and deposition in coal combustion. In addition, drop tubes (hereafter DT) or entrained flow reactors (hereafter EFR) have been used in many works on pulverized coal combustion and, in particular, for the investigation of ash deposition phenomena. A few examples of studies of this kind are those of Gibb [10], Haas *et al.* [10], Helble *et al.* [11], Hutchings *et al.* [12], Rushdi *et al.* [13] and Russell *et al.* [14]. DT and EFR might provide very valuable information that could be used to anticipate problems in large boilers or to select the most convenient fuels or operating conditions. An important drawback is, however, the fact that the use of EFR facilities for that purpose still only provides macroscopic information about ash deposition, and cannot explain ash deposition mechanism(s) from a microscopic viewpoint.

Ash deposition rate is proposed to be controlled by the summation of five processes: inertial impaction (*I*), eddy impaction (*E*), thermophoresis (*T*), condensation (*C*), and chemical reaction (*R*) [15], as described in Equation (1):

$$\frac{dm}{dt} = I \cdot G + E + T + C + R \tag{1}$$

Inertial impaction takes place when the momentum of the particle toward the tube is large enough to overcome drag forces produced by fluid flow. As a result, particles pass through the boundary layer and stagnation zone, and impact the tube. Eddy impaction involves fine ash particles that are entrained in turbulent flows. Eddy impaction is relevant only to small particles. Thermophoresis is the process of particle motion in a gas due to local temperature gradients. Condensation is the mechanism by which vapors are collected on cooled heat transfer surfaces. Heterogeneous chemical reactions between the gas and either the existing deposit materials or the deposit surfaces can also add or remove mass.

Among the five ash deposition mechanisms, researchers have focused on inertial impaction for its major contribution to deposit mass accumulation [15–17]. The impaction is described by two parameters: (1) impaction efficiency (η), (2) capture efficiency (G). The impaction efficiency is defined as the ratio of particles impacting a surface to the number of total particles flowing across the projected surface area. The product of particle flux, projected surface area, and impaction efficiency, η is I. The capture efficiency is defined as ratio of attached particles to total particles impacting the surface.

The particle capture is a process dependent on the physical properties of the impacting particle and surface. Dahneke studied the normal impact of polystyrene latex microspheres with surfaces under

vacuum conditions [18–20]. He found that particles with an initial velocity less than a critical value were captured by the surface. The particles with an initial particle velocity faster than this threshold velocity rebounded from the substrate. Unfortunately, limitations of the bounce cell design prevented measurements down to near-critical velocity, where energy loss owing to surface adhesion dominates. Rogers and Reed measured critical impact velocity for large (15–40 μm) copper microspheres using a high speed camera. They evaluated an elastic-plastic impact model for particle adhesion [21].

However, one of the most comprehensive experimental investigations for small particles impacting surfaces at normal incidence is that of Wall *et al.* [22]. They measured incoming and rebounding particle velocities to within several particle diameters of the impaction surface with a laser Doppler velocimetry system. At low velocity (<20 m/s), the ratio of rebound to impact velocity was sensitive to target material, decreasing with impact velocity due to the adhesion surface energy, while for higher particle velocities, the ratio of rebound to impact velocity was insensitive to the target material.

Measurements of individual normal and oblique impacts of microspheres with planar surfaces are described and analyzed by Dunn *et al.* [23]. Their experimental results were similar in behavior to the previous studies using monodisperse spheres. Beek *et al.* investigated rebound characteristics of 50 μm particles impacting a powdery layer [24]. This was studied by impaction experiments of glass particles on different types of glass layers (powdery *vs.* glued), under various impact angle conditions (ranging from 0° to 30°) and with different incident velocities (ranging from 0.5 to 1 m/s). Besides, a 2-body collision model was developed to simulate the rebound characteristics. From a comparison between the experimental results and the model, it is shown that the 2-body approach to model the rebound characteristics of particles impacting a powdery layer is valid. Kim and Dunn [25] provided direct imaging results of microparticle collisions, whereby 40 μm diameter Ag-coated glass particles were dispersed and vertically dropped onto a silica target plate. The collisions under standard atmospheric conditions were resolved with a digital high-speed technique using black-light illumination.

Despite the above developments on the study of ash deposition for EFR and the impact problems of particles with a substrate, there are still many important issues that remain unresolved. For example, practical ash particles impact a flat and powdery substrate. In addition, the effects of the temperatures of particle and substrate on the rebound characteristic of particles need to be investigated in detail. Therefore, the present work provides a basis for investigating the rebound behavior of fly ash particles impacting normally on a flat substrate in a high temperature environment. Section 2 discusses the experimental set-up comprising the impact unit, the image analysis and the fly ash particle component analysis. The digital high-speed technique was used to determine particle incidence and rebound velocity magnitude from digital images. The theoretical background of impacts between fly ash particles and planar surfaces are given in Section 3. The experimental results are compared to the theoretical analysis and discussed in Section 4. Conclusions are given in Section 5.

2. Experimental System and Approach

2.1. Experimental Apparatus

An experimental facility was developed to investigate the impact of fly ash particles with planar surfaces. A schematic of the experimental apparatus with the configuration used for normal impact measurements is shown in Figure 1. Nitrogen is drawn through a fluidized bed particle generator and

carries the fly ash particles into the test section (the incident velocity was 0.1 to 16 ms^{-1}). The test section includes a planar surface whose diameter is 2 mm. The planar surface was made of stainless steel and was oriented at parallel with the horizontal flow. The incidence and rebound normal velocity components of fly ash particles are recorded using a digital high-speed camera (Phantom V12.1, Vision Research Inc., Wayne, NJ, USA). Optical lenses are attached to the camera to achieve enough magnification to resolve individual particle motion. The camera output is connected to a digitizer and a frame grabber in a personal computer for image analysis. All experiments are conducted at a temperature of ~22 °C and a relative humidity of 25% ± 3%. Experimental repeatability was assessed by repeating the experiment under the same conditions.

Figure 1. Schematic of the experimental configuration with the high-speed camera system used in the normal impact experiments.

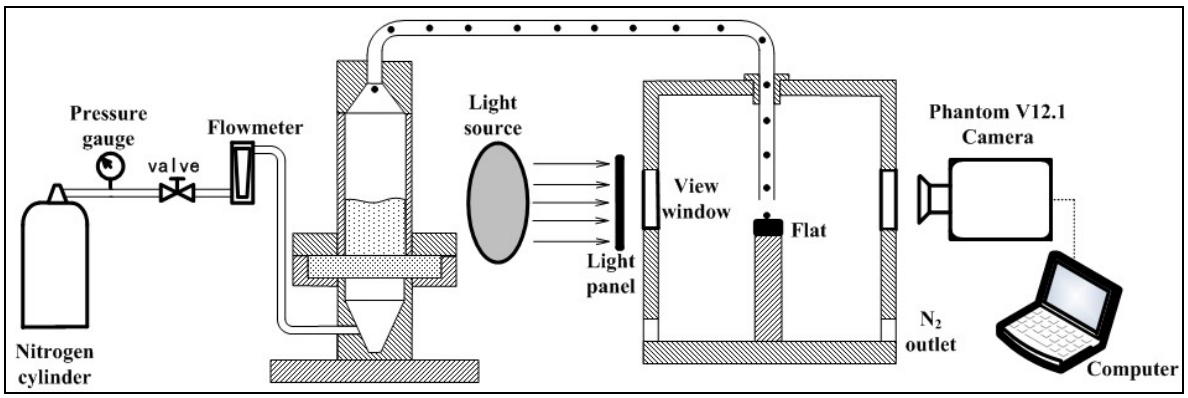

2.2. The Shooting Region

The vertical distance between the outlet of the particle export pipe and the target surface is about 2 mm. Diameter of the target surface is 2 mm. In order to determine the shooting region of the particle impact process, the velocity field between outlet of the particle export pipe and the target surface has been calculated using the commercial software package FLUENT (ANSYS Inc., Berkeley, CA, USA). Meanwhile, particle impact experiments were carried out. The experimental results and numerical simulation results are compared to determine the shooting region. Numerical computational region, boundary condition and the mesh of the computational model are shown in Figure 2.

Due to the high flow shear stresses near the target surface, refined meshes are used in the wall boundary. When the N_2 inlet volume flow rate is 140 and 1200 mL/min, the outlet velocity magnitude of the particle export pipe is 0.74 and 6.37 m/s, respectively. Furthermore, the Reynolds numbers are 92.54 and 842.1, respectively. Therefore, the flow field is laminar. In the present study, the particles are carried by nitrogen; all experiments are conducted under atmospheric room pressure at room temperature conditions. Therefore, the computational model can be assumed to be steady, incompressible flow.

The shooting region initially selected is indicated by the dotted region in Figure 2a. The fly ash particle diameter is about 88 μm. Two incident velocities are obtained by the experiments, which are 2.432 and 8.6 m/s, respectively. The rebound velocities are 0.591 and 2.262, respectively.

Figure 3 shows the velocity field under different outlet velocity magnitudes of the particle export pipe. The fluid velocity close to the target surface increased with increasing outlet velocity of the particle export pipe. The fluid velocities at locations i =1, 2, …, 6 are shown in Table 1.

Figure 2. (**a**) The numerical computational region and boundary condition and, (**b**) the mesh of the computational model.

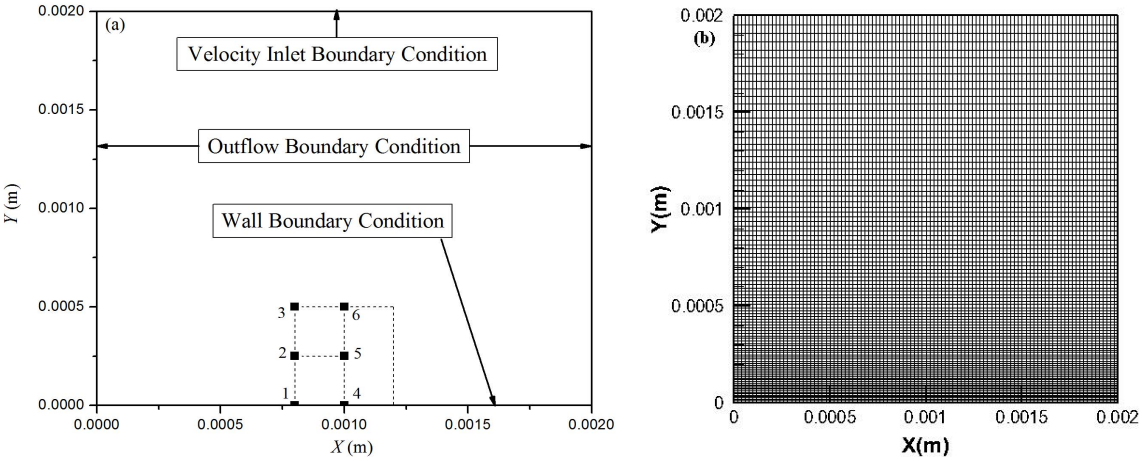

(a) **(b)**

Figure 3. The velocity field under different outlet velocity magnitudes of the particle export pipe. (**a**) The outlet velocity magnitude of particle export; and (**b**) the outlet velocity magnitude of particle export pipe is 0.74 m/s. Pipe is 6.37 m/s.

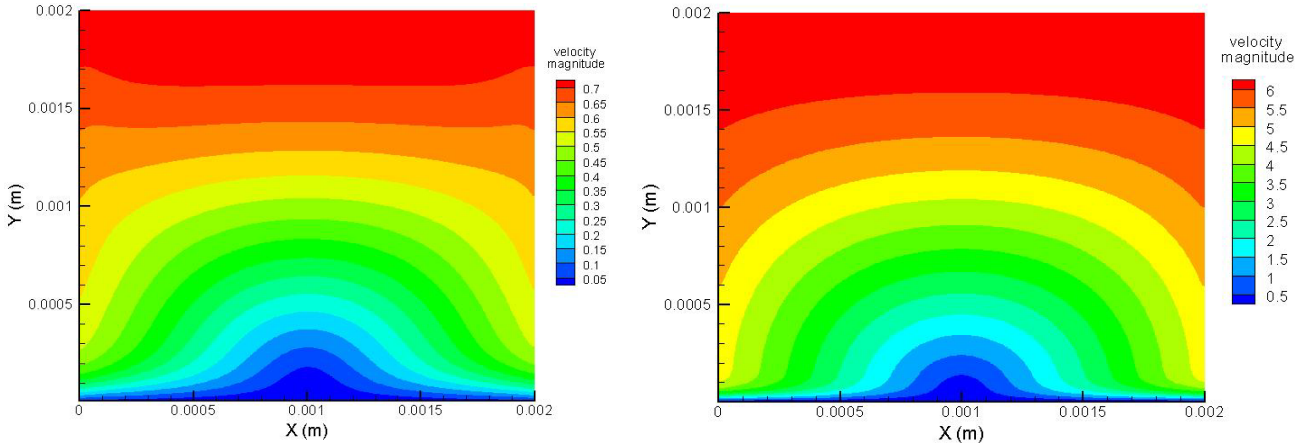

(a) **(b)**

Table 1. Effect of fluid drag force on particles (d_p = 88 μm).

N_2 flow rate (mL/min)	Normal incident velocity (m/s)	Normal rebound velocity (m/s)	Location *i*	Fluid velocity for *i* (m/s)	Drag force of incident process F_d (*nN*)	Drag force of rebound process F_d (*nN*)
140	2.432	0.591	1	0.0000	−33.54	−8.15
			2	0.1343	−31.69	−10.00
			3	0.2467	−30.14	−11.55
			4	0.0000	−33.54	−8.15
			5	0.0841	−32.38	−9.31
			6	0.2207	−30.50	−11.20

Table 1. *Cont.*

N_2 flow rate (mL/min)	Normal incident velocity (m/s)	Normal rebound velocity (m/s)	Location *i*	Fluid velocity for *i* (m/s)	Drag force of incident process F_d (*nN*)	Drag force of rebound process F_d (*nN*)
1200	8.6	2.262	1	0.0000	−118.62	−31.20
			2	1.4279	−98.92	−50.89
			3	2.4171	−85.28	−64.53
			4	0.0000	−118.62	−31.20
			5	1.0529	−104.09	−45.72
			6	2.2429	−87.68	−62.13

The expression for drag force [26], F_d, on a spherical particle is based on a modified form of the classic solution given by Stokes as:

$$F_d = -3\pi d_p \mu C(v-u) \tag{2}$$

where u is the velocity that the fluid would have had at the particle centroid had the particle not been present and v is the particle velocity. Here C is a friction factor which can be expressed as the product of various correction factors as:

$$C = C_I C_F C_C \tag{3}$$

The methods for calculating C_I, C_F and C_c are described in detail in [26], so the present paper will not described them in detail. The drag forces of the incidence process and of the rebound process are shown in Table 1, the negative sign "–" indicates the opposite direction of the particle motion.

Based on the soft sphere model, the particle-wall interaction equation is given by:

$$m^* \frac{d^2\delta}{dt^2} + \eta \frac{d\delta}{dt} + F_{tot} = 0 \tag{4}$$

where F_{tot} is the total force of a particle; η is the corresponding damping coefficient of F_{tot}; and δ is the overlap. For a particle with mass m_1 impacting normally with a particle with mass m_2, m should be replaced with the effective mass m^* defined by $m^* = (m_1^{-1} + m_2^{-1})^{-1}$, which reduces to m_1 if the second particle is a flat substrate, *i.e.*, $m_2 = +\infty$.

A similar form of the motion equation was adopted in Brach and Dunn [27] which was also used in their following works (e.g., [28,29]). The total force considers repulsive force and attractive force. The expressions of the repulsive force F_r^{BD} and the attractive force F_a^{BD} give:

$$F_r^{BD} = \frac{4}{3} E^* R^{*1/2} \delta^{3/2} \tag{5}$$

while the attractive force is idealized by a line force at the perimeter of the contact area as:

$$F_a^{BD} = -2\pi af = -2\pi f R^{*1/2} \delta^{1/2} \tag{6}$$

$$f = \left(\frac{6w^2 R^* E^*}{\pi}\right)^{1/3} \tag{7}$$

The discrete form of Equation (4) is given by:

$$\frac{\delta_i - 2\delta_{i+1} + \delta_{i+2}}{\Delta t^2} + \frac{\eta}{m_1}\frac{\delta_{i+1} - \delta_i}{\Delta t} + \frac{4}{3}\frac{E^* r_1^{1/2}}{m_1}\delta_{i+1}^{3/2} - \frac{2\pi f r_1^{1/2}}{m_1}\delta_{i+1}^{1/2} = 0 \quad (8)$$

Equation (4) is now used to calculate the variation of overlap and of total force with contact time. The curves of overlap with contact time and of the total force with contact time are shown in Figure 4. Where the total force of incident velocity of 1.93 m/s is 22 mN, which increases to 105 mN for the incident velocity of 9.078 m/s under the maximum overlap conditions. The total forces are much larger than the fluid drag force, therefore, the fluid force can be ignored when the particle is close to the target surface, and the dotted line in Figure 2a can be used as the shooting region.

Figure 4. (**a**) The curves of overlap with contact time and (**b**) the curves of total force with contact time.

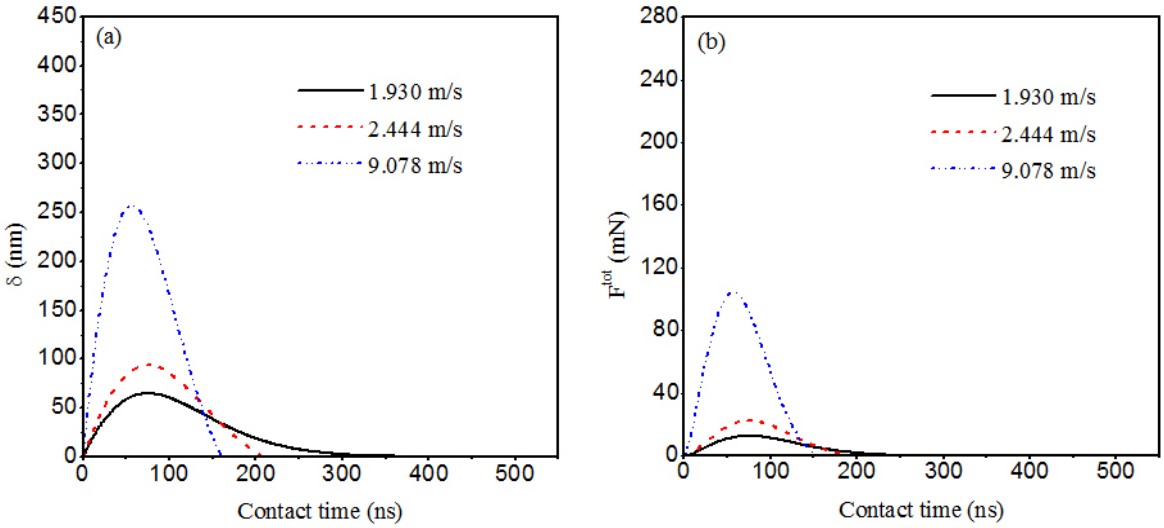

2.3. Particle Generator

In these experiments, the fly ash particles were dispensed using a fluidized bed particle generator. The fluidized bed particle generator consists of a wind chamber, and air distribution plate, bed, feeding systems, *etc.* In order to disperse the fly ash particles efficiently, a particle size range of 150–200 μm copper beads are used as bed material. In addition, these copper beads can also eliminate static electricity. Filtered compressed nitrogen is used as the fluidizing gas. Before running the fluidized bed particle generator device, fly ash particles and copper beads are put on this device in accordance with a certain ratio. Then, compressed nitrogen gas gets into the bed through the wind chamber. The terminal velocity of fly ash particles is less than 0.1 m/s, and the terminal velocity of copper beads is greater than 20 m/s. However, the nitrogen apparent speed is 0.1 to 16 m/s, so the fly ash is taken out of bed by the nitrogen. The particles form a stable aerosol to continue the upward movement, which can be extracted by an aerosol export pipe. As a result, the fly ash particles were directed downward in a straight trajectory onto the target surface.

2.4. Particles

In the present study fly ash particles were sampled from the in dust in front of the boiler of a power plant and used as impacting particles. Before carrying out an experiment, the particles were stored in a

stove at 80 °C to minimize agglomeration problems. The microscopic morphology of the fly ash particles is obtained by Scanning Electron Microscopy (SEM). The microscopic morphology of the fly ash particles is irregular spheres, as shown in Figure 5.

The fly ash was sieved to separate the different size ranges. The crystal phases and weight percentages of the fly ash was investigated using X-ray diffraction (XRD) analysis. The fly ash was divided into the sample for XRD. Its scans were from 10° to 70° at a scanning speed of 1.25°2θ/min. Through XRD analysis, the crystallinity data of fly ash particles can be obtained. Then the data can be used to estimate the Young's modulus of fly ash particles [30].

Figure 5. The microscopic morphology of the fly ash particles.

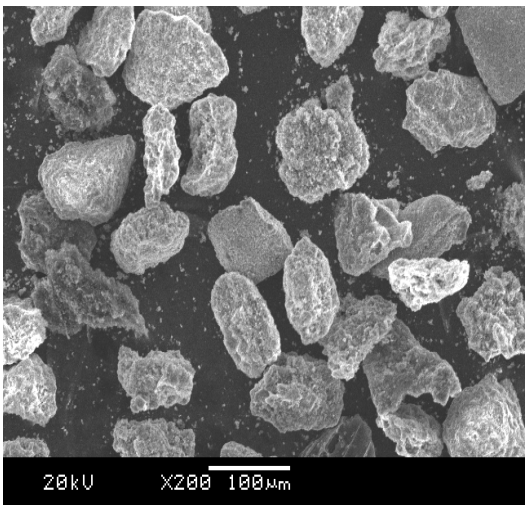

From the XRD analysis, it is found that the fly ash is mainly made up of either quartz, Q (SiO_2) or mullite, M ($3Al_2O_3 \cdot 2SiO_2$). The weight percentage of crystallinity was calculated based on the XRD result which was obtained using the MDI Jade 5.0 software (Materials Data Inc., Livermore, CA, USA). This paper assumes that the crystalline phase of the fly ash only consists of quartz and mullite. Since the density of quartz, mullite, and glassy phase are 2.65, 2.80 and 2.5 $g \cdot cm^{-3}$ [31], respectively, then the volume fractions of quartz, mullite, and glassy phase can be obtained. The volume fractions of all crystalline phases (quartz and mullite) are obtained from the quantitative XRD analysis results. The volume fractions of total crystalline phase, quartz, and mullite are 49.28%, 1.65%, 47.63%, respectively.

The modulus of fly ash was estimated using the parallel model of rules of mixtures [30]. The parallel model can be written as:

$$E_{fly\ ash} = E_g V_g + E_m V_m + E_q V_q \tag{9}$$

where E is the Young's modulus; and V is volume fraction; and subscripts g, m, and q denote glass, mullite, and quartz, respectively. The modulus of quartz and mullite were taken as 94 and 230 GPa, respectively, and the average moduli of the glassy phase was taken as 73 GPa [32], so the Young's modulus of the fly ash particle is calculated to be 148 GPa.

2.5. Image Analysis

The course of the impact is recorded using a digital high-speed camera (Phantom V12.1) at a frame rate of 80,000 frames/s, and an exposure time of 11.93 μs. To determine the impact and rebound

velocities accurately, the camera is equipped with a Tokina AT-X M 100 PROD lens (Kenko Tokina Co. Ltd., Tokyo, Japan). To track an incident and a rebound particle passing through this domain, a fiber optic solar light source (XD-300 xenon lamp, Alltion Co. Ltd., Guangxi, China) was used to backlight the fly ash particle impact events. An example of a recorded image with a resolution of 256 × 128 is given in Figure 6. In order to reduce the effect of the particle shape and the fluid drag force on the accuracy of the velocity measurements, incident velocities are determined from the distance of successive blobs 19–20 in Figure 6, and rebound velocities are determined from the distance of successive blobs 22–23 in Figure 6.

Figure 6. Typical recorded image for the impact of a fly ash particle on a flat surface.

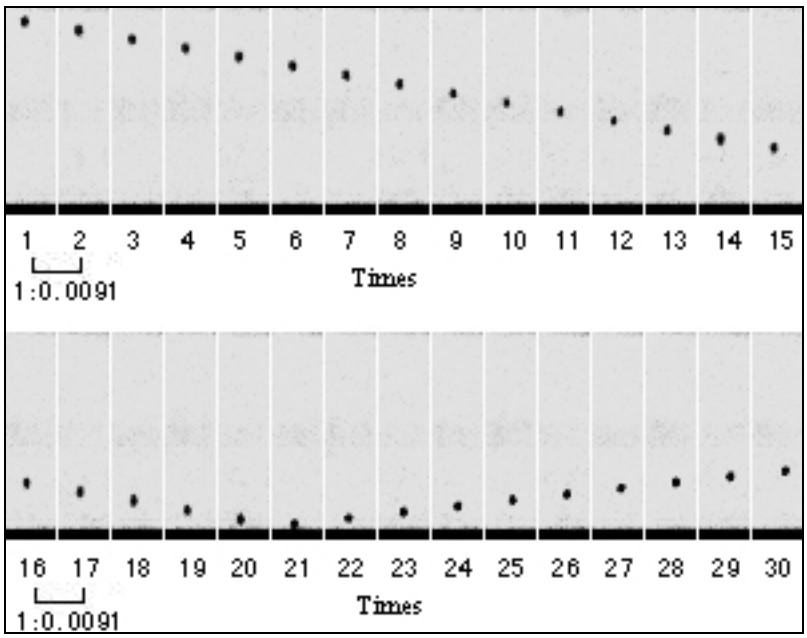

Due to the fact the images of the shot pictures appeared fuzzy after zooming, direct measurement of the particle diameter will cause large errors. In the present paper, the digital image processing imtool function of the MATLAB (MathWorks, Natick, MA, USA) software is used to obtain the particle diameter. Firstly, the appropriate tolerance is selected to measure the pixel values of target, whose size is known. Then, the value of particle pixel area is measured to obtain the particle diameter by scaling:

$$k = \frac{d_{f,r}}{d_{f,i}} \tag{10}$$

where k is the proportionality coefficient (μm/pixel); $d_{f,r}$ is the actual size of targets (μm); $d_{f,i}$ is the pixel values of target (pixel):

$$d_{p,i} = \sqrt{\frac{4S_{p,i}}{\pi}} \tag{11}$$

$$d_{p,r} = k \times d_{p,i} \tag{12}$$

where $d_{p,i}$ is the pixel values of particle; $d_{p,r}$ is the actual size of the particle (μm); $S_{p,i}$ is the value of particle pixel area (pixel^2).

3. Theoretical Background

3.1. Energy Balance

The fly ash particles have elastic-plastic particle properties. The interaction between the particle and planar surface is considered to have two stages. The first stage starts at the moment of initial contact of the bodies and is characterized by the deformation of fly ash particle being purely elastic. As the impact progresses the pressure between the two bodies increases until the peak pressure reaches the elastic yield limit Y of the fly ash particle. The second stage of the impact, which continues until the impacting bodies have zero relative velocity, is characterized by the growth of a region of plastic deformation in the fly ash particle. It is assumed that the elastic yield limit remains constant throughout the impact.

A schematic diagram of the impact process of fly ash particle with planar surfaces treated as a simple energy balance is shown in Figure 7. An energy balance for the impact is:

$$K_i = K_e + K_{pe} + K_p \tag{13}$$

where K_i is the kinetic energy for the incoming particle; K_e is the elastic energy stored in the area of elastic deformation; K_{pe} is the elastic energy stored in the area of plastic deformation; K_p is the impact energy dissipated due to plastic deformation.

Figure 7. A diagram of the particle bounce process as a simple energy balance for normal impacts showing (**a**) the incident particle approaching the surface, (**b**) the particle at full compression before rebound, and (**c**) the rebounding particle.

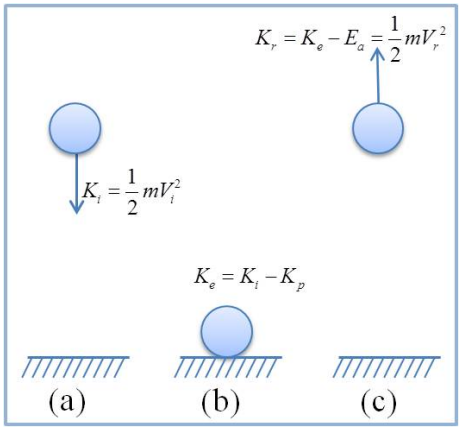

The Hertz equations are applied for only elastic impacts. The elastic yield limit Y can be utilized to determine the limiting velocity V_y, above which plastic deformation begins to occur. V_y is given by [21,33]:

$$V_y = (2\pi/3K)^2(2/5\rho)^{1/2}Y^{5/2} \tag{14}$$

where ρ is the density of the fly ash particle and:

$$K = 4/[3(k_1 + k_2)] \tag{15}$$

with $k_i = (1-v_i^2)/\xi_i$, where v_i is the Poisson ratio and ξ_i is the Young's modulus for the material of object i. The limiting velocity is determined by the bulk material properties and is independent of particle size.

The energy stored in elastic deformations is just the limiting kinetic energy, $K_y = mV_y^2/2$. An expression derived by Bitter for the impact energy dissipated due to plastic deformation, K_p, can be expressed as [21,33]:

$$K_p = [(K_i - K_y/16)^{1/2} - (15K_y/16)^{1/2}]^2 \quad (16)$$

From energy conservation, Rogers and Reed determined the necessary condition for particle rebound on impact with a surface to be [21]:

$$K_i - K_p > E_a \quad (17)$$

where $(K_i - K_p)$ is the stored elastic energy available elastic energy for rebound; and E_a is the total adhesion energy from the equilibrium circle of contact. If the available elastic energy $(K_i - K_p)$, is less than the adhesive energy, E_a, then the particle will always adhere. If the available elastic energy is greater than the adhesive energy then the particle may rebound. The total adhesive energy has been presented by Johnson *et al.* [34] as the sum of a mechanical energy E_m and a surface energy E_s, such as:

$$E_a = E_m + E_s \quad (18)$$

The calculation method of E_m, E_s was in detail discussed in the literature [11,21], so the present paper will not describe it.

3.2. Energy Dissipation

Figure 8 shows the force displacement relationship as defined by Thornton and Ning [35]. According to Johnson-Kendall-Roberts (JKR) theory, the contact of two colliding bodies commences when the overlap exceeds zero (point A in Figure 8), due to Van der Waals attractive force. When the contact force reaches a maximum value (point B in Figure 8) the particle velocity has been reduced to zero and the incoming stage is complete. In the recovery stage, all the work done during the loading stage has been recovered when point A is reached during the recovery stage. However, at this point, when $\delta = 0$, the particle remains adhered to the surface and further work is required to separate the surfaces. Figure 8 shows that separation occurs at point C and hence the work required breaking the contact, which results in an energy loss given by:

$$W_s = 7.09(\gamma^5 R^4 E^{-2})^{1/3} \quad (19)$$

where γ, R and E are the surface adhesive energy, reduced particle radius and Young's modulus, respectively [35]. When the energy losses are neglected due to elastic wave propagation, the only work dissipated during a collision is the work done of separating the surfaces W_s. While the particle is captured, the critical impact velocity v_s is obtained:

$$V_s = (14.18/m_p)^{1/2}(\gamma^5 R^4 E^{-2})^{1/6} \quad (20)$$

below which the impact results in a final capture. For a particle impacting a flat surface, this leads to:

$$V_s = 1.84(\gamma/R)^{5/6}/(\rho^3 E^2)^{1/6} \quad (21)$$

Figure 8. Schematic illustration of the force displacement relationship.

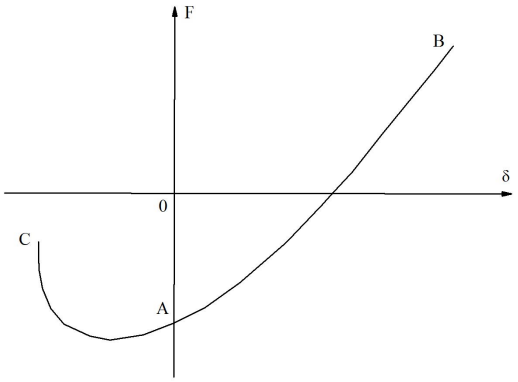

By noting $V_s \infty R^{-5/6}$, it is predicted that *Ws* will play an increasingly important role in describing the behavior of small particles. Liu *et al.* [36] showed that *Ws* is introduced into the total energy loss once the contact is established, and refer to *Ws* as the first-contact energy loss for simplicity.

4. Results and Discussion

4.1. Normal Coefficient of Restitution

In this paper, the rebound-to-incident normal velocity component ratio ($v_{r,n}/v_{i,n}$) is denoted as the normal coefficient of restitution (e_n). Figure 9 displays the normal coefficient of restitution (e_n) *versus* the incident velocity (v_{in}) for the normal impact of fly ash particles diameter of 60–90 μm. Below ~2.0 m/s, the normal restitution coefficient rapidly increases with increasing v_{in}, and the slope $\partial e_n/\partial v_{i,n}$ decreases with increasing v_{in} for all three cases. This trend is consistent with the results of previous investigators [24], and serves to illustrate the increasing role of adhesion at lower velocities.

Figure 9. The normal restitution coefficient, e_n, *versus* the incident normal velocity component, v_{in}, for the normal impact of fly ash particles diameter of 60–90 μm.

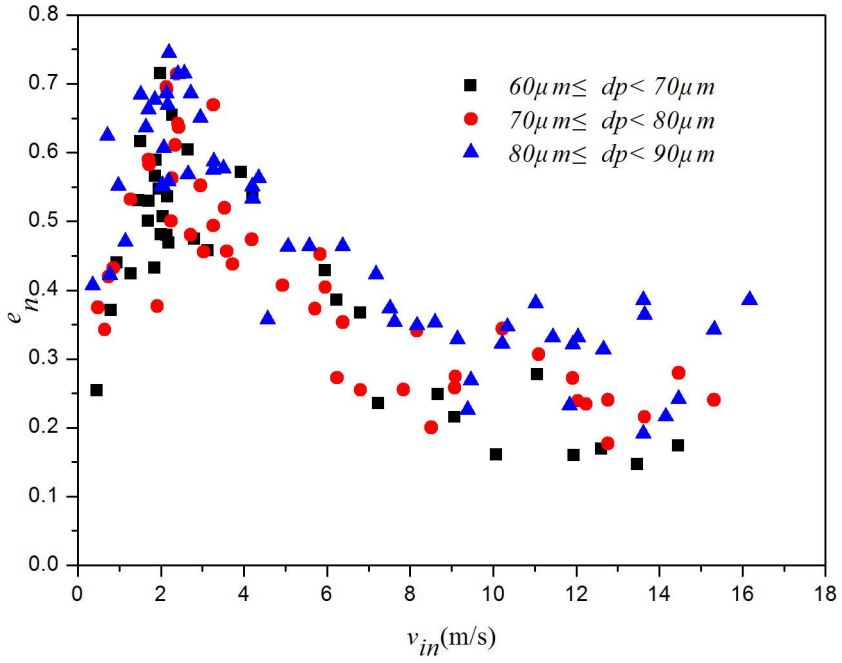

Further, the normal restitution coefficient at the same initial velocity for the three kinds of particle size range increases with increasing particle diameter. Above ~2.0 m/s, the normal restitution coefficient rapidly decreases with increasing v_{in}. At the same initial velocity, the normal restitution coefficient increases with increasing particle diameter. The causes for these variations are now discussed by considering an example case.

The sample mean values of the normal restitution coefficient *versus* the initial normal velocity are shown in Figure 9 for the normal impact of fly ash particles diameter of 75 ± 5 μm. The bounds vary by approximately ±12% at the higher incident velocities and increase to approximately ±35%−50% at lower incident velocities. Comparing Figure 10 with Figure 9, the trend of the normal restitution coefficient *versus* incident velocity is much clearer. Firstly, the normal restitution coefficient increases with increasing incident velocity, and then the normal restitution coefficient decreases with increasing incident velocity. The Rogers and Reed model was solved for a copper particle of 50 μm diameter hitting a massive steel plate at different impact speeds by Adb-Elhady *et al.* [37]. The copper particle was chosen to represent the soft fouling particle in gasified biomass and the steel plate to represent the heat exchanger tubes. They analysed plastic energy loss, the stored elastic energy and the ratio between them at different impact velocities. It can be concluded that the plastic energy loss obviously increases with increasing incident velocity in comparison to the stored elastic energy.

Figure 10. The sample mean values of normal restitution coefficient, e_n, *versus* the incident normal velocity component, v_{in}, for the normal impact of fly ash particles diameter of 75 ± 5 μm.

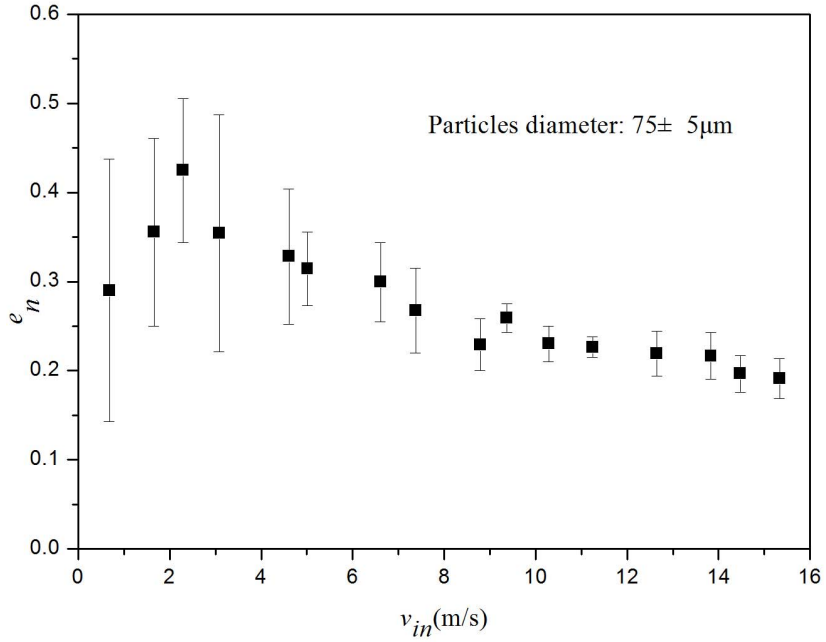

The elemental composition of fly ash particles includes SiO_2, Al_2O_3, Fe_2O_3, CaO, MgO, SO_3, Na_2O, K_2O, *etc.* The micron size fly ash can undergo plastic deformations at low collision velocity. The Rogers and Reed model [21] is used to validate that plastic deformation needs to be taken into account. In this paper, the Rogers and Reed model was solved for a fly ash particle of diameter 75 μm hitting a planar steel plate at different impact velocity and the results are depicted in Figure 10. The steel plate was chosen to represent the heat exchangers tube. The incident kinetic energy K_i, the plastic energy loss K_p, the stored elastic energy $K_e + K_{pe}$ are shown in Figure 11.

Figure 11 shows that the significance of the plastic energy loss in comparison to the stored elastic energy, which is transformed into rebounding kinetic energy during the restitution phase can be clearly seen. It can be concluded that for velocities relevant in the flue gas pipelines of pulverized coal boilers, plastic deformation of colliding particles play an important role in the particles' post-collision behavior. Below ~2.0 m/s, the values of K_i, K_p, $K_e + K_{pe}$ is very close. Above 2.0 m/s, the plastic energy loss and stored elastic energy gradually increase with increasing particle incident velocity v_{in}, the difference between K_p and $K_e + K_{pe}$ increases slightly with increasing v_{in}. Therefore, that the incident velocity of fly ash particle increases lead to the plastic energy loss plays an important role in the fly ash particle collisions with planar surfaces. Furthermore, the normal coefficient of restitution decreases with increasing incident velocity of fly ash particles.

Figure 11. The incident kinetic energy K_i, the plastic energy loss K_p, the stored elastic energy $K_e + K_{pe}$ for fly ash particles of 75 μm diameter hitting a planar steel plate at different impact speeds.

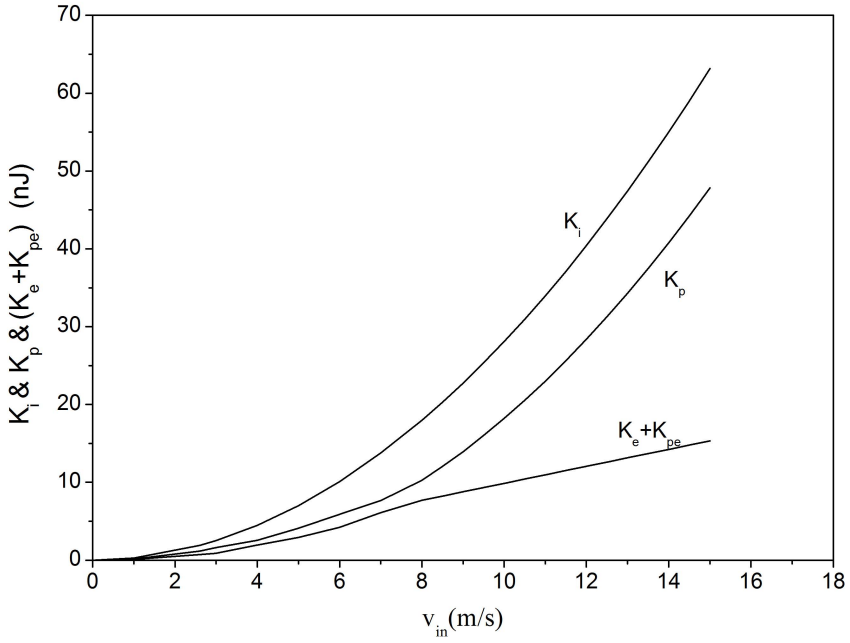

4.2. The Critical Velocity for Particle Capture

The critical velocity v_s, is a key parameter for the dynamic impact. Incident velocity below v_s makes the particle be finally captured, leading to particle deposition on walls or formation of particle aggregates. The magnitude of v_s reflects the relative strength of adhesion.

It is known that the viscoelastic effect and the plastic deformation play import roles in energy loss during low-velocity impact and high-velocity impact, respectively [22]. For the incident velocity close to the critical velocity, the plastic effect is considered to be negligible.

The data for critical velocity as a function of particle size obtained in this study are plotted in Figure 12 with other relevant data from the literature for comparison [22]. The particle diameters of the present study are higher than those used in the other literature. The slopes of the lines through the present results are in the same range as those of Rogers and Reed [21] for impacts between copper and harder materials. A slope significantly less than unity occurred only for the results of Esmen [22].

These measurements were unusual due to a coating of carbon on the impaction surface which was removed by the particles during impact. In Figure 12, the critical velocity data collected in this study for impacts between fly ash particle and steel. The critical velocity decreases with increasing incident particle diameter. The critical velocity determined solely by the first-contact energy loss, is proportional to $d_p^{-5/6}$ and therefore gets larger for smaller particles. For instance, as in the present work, the critical velocity of the particle with diameter of 85 μm is 0.19 m/s, which increases to 0.42 m/s for the particle with diameter of 65 μm.

Figure 12. Comparison of available data relating critical velocity to particle size.

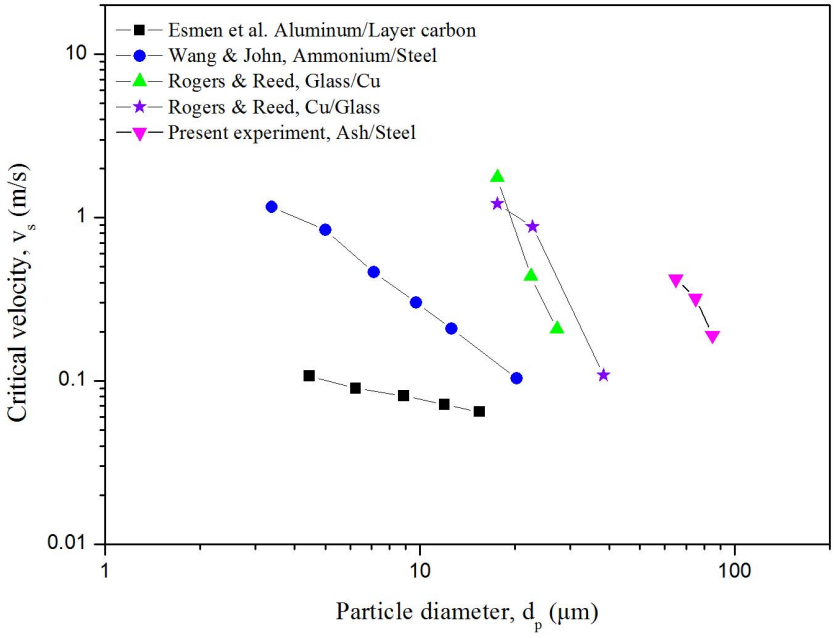

5. Conclusions

This paper presented the results from an extensive experimental program to investigate the effect of particle incident velocity, particle diameter on the normal restitution coefficient, and of particle diameter on the critical velocity. The effect of the incident normal velocity, particle diameter on the normal restitution coefficient was also examined. The experimental systems were designed to study the normal fly ash particle impacts with a planar surface under an atmospheric environment. Impacts have been carried out between 60 μm < d_p < 90 μm fly ash particles and a planar steel surface at an incident velocity of 0.1–16 m/s, while the impact angle maintains normal. The main conclusions to emerge from this work are as follows:

(1) The ease of use of the experimental equipment enabled a large number of tests to be conducted.
(2) The incident particle velocity is the most significant variable in terms of the normal restitution coefficient. When the fly ash particles impact with a planar surface, the normal restitution coefficient rapidly increases with increasing incident velocity for the incident velocity is less than the yield velocity, and rapidly decreases with increasing incident velocity for the incident velocity is greater than the yield velocity. The reason is that the increases in incident velocity of fly ash particles lead to the plastic energy loss that plays an important role in the fly ash particle collisions with a planar surface. Furthermore, the normal coefficient of restitution

decreases with increasing incident velocity of fly ash particles when the incident velocity is greater than the yield velocity.

(3) The critical velocity determined solely by the first-contact energy loss, is proportional to $d_p^{-5/6}$ and therefore gets larger for smaller particles. For instance, as the present work, the velocity v_c of the particle with diameter of 85 μm is 0.19 m/s, which increases to 0.42 m/s for the particle with diameter of 65 μm.

Therefore, using fly ash particle impact studies, the results from this paper have provided valuable information on how to minimize ash deposition in a boiler system. Coupling these results with the mathematical model developed by Roger and Reed [21] will enable the ash deposition process to be predicted.

Acknowledgements

The authors acknowledge the support to this work by the National Natural Science Foundation of China (NSFC Grant No. 51006055) and by the Fundamental Research Funds for the Central Universities [No. DUT11RC (3) 27].

Conflict of Interest

The authors declare no conflict of interest.

References

1. Lokare, S.S.; Dunaway, J.D.; Moulton, D.; Rogers, D.; Tree, D.R.; Baxter, L.L. Investigation of ash deposition rates for a suite of biomass fuels and fuel blends. *Energy Fuels* **2006**, *20*, 1008–1014.
2. Zbogar, A.; Frandsen, F.; Jensen, P.A.; Glarborg, P. Shedding of ash deposits. *Prog. Energy Combust. Sci.* **2009**, *35*, 31–56.
3. Srinivasachar, S.C.; Senior, L.; Helble, J.J.; Moore, J.E. A fundamental approach to the prediction of coal ash deposit formation in combustion systems. *Proc. Combust. Inst.* **1992**, *24*, 1179–1187.
4. Vuthaluru, H.B.; Wall, T.F. Ash formation and deposition from a Victorian brown coal-modelling and prevention. *Fuel Process. Technol.* **1998**, *53*, 215–233.
5. Raask, E. *Mineral Impurities in Coal Combustion*; Hemisphere Publishing Company: Washington, DC, USA, 1985; pp. 189–201.
6. Walsh, P.M.; Sayre, A.N.; Loehden, D.O.; Monroe, L.S.; Beer, J.M.; Sarofim, A.F. Deposition of bituminous coal ash on an isolated heat exchanger tube: Effects of coal properties on deposit growth. *Prog. Energy Combust. Sci.* **1990**, *16*, 327–345.
7. Baxter, L.L. Influence of ash deposit chemistry and structure on physical and transport properties. *Fuel Process. Technol.* **1998**, *56*, 81–88.
8. Beer, J.M.; Sarofim, A.F.; Barta, L.E. From Coal Mineral Properties to Fly Ash Deposition Tendencies. In *Transformations and Ash Deposition during Combustion*, Proceedings of the Engineering Foundation Conference on Inorganic Transformations and Ash Deposition During Combustion, Palm Coast, FL, USA, 10–15 March 1991; Benson, S.A., Ed.; American Society of Mechanical Engineers: New York, NY, USA, 1992.

9. Benson, S.A.; Jones, M.L.; Harb, J.N. Ash Formation and Deposition. In *Fundamentals of Coal Combustion*; Smoot, L.D., Ed.; Elsevier Science: New York, NY, USA, 1993; pp. 399–373.
10. Gibb, W.H. The UK Collaborative Research Programme on Slagging Pulverized Coal-Fired Boilers: Summary of Findings. In *Applications of Advanced Technology to Ash-Related Problems in Boilers*, Proceedings of the Engineering Foundation Conference on Applications of Advanced Technology to Ash-Related Problems in Boilers, Waterville Valley, NH, USA, 16–21 July 1995; Baxter, L., DeSollar, R., Eds.; Kluwer Academic Publisher: Dordrecht, The Netherlands, 1996.
11. Hass, J.; Tamura, M.; Weber, R. Characterisation of coal blends for pulverized fuel combustion. *Fuel* **2001**, *80*, 1317–1323.
12. Helble, J.J.; Srinivasachar, S.; Boni, A.A. Factors influencing the transformation of mineral matter during pulverized coal combustion. *Prog. Energy Combust. Sci.* **1990**, *4*, 267–279.
13. Hutchings, I.S.; West, S.S.; Williamson, J. An Assessment of Coal Ash Slagging Propensity Using an Entrained Flow Reactor. In *Applications of Advanced Technology to Ash-Related Problems in Boilers*, Proceedings of the Engineering Foundation Conference on Applications of Advanced Technology to Ash-Related Problems in Boilers, Waterville Valley, NH, USA, 16–21 July 1995; Baxter, L., DeSollar, R., Eds.; Kluwer Academic Publisher: Dordrecht, The Netherlands, 1996.
14. Manton, N.J.; Williamson, J.; Riley, G.S. Changes in Slagging Behavior with Composition for Blended Coals. In *Impact of Mineral Impurities in Solid Fuel Combustion*; Springer: New York, NY, USA, 2002.
15. Baxter, L.L. Ash deposition during biomass and coal combustion: A mechanistic approach. *Biomass Bioenergy* **1993**, *4*, 85–102.
16. Nielsen, H.P.; Baxter, L.L.; Sclippab, G.; Morey, C.; Frandsen, F.J.; Dam-Johansen, K. Deposition of potassium salts on heat transfer surfaces in straw-fired boilers: A pilot-scale study. *Fuel* **2000**, *79*, 131–139.
17. Nielsen, H.P.; Frandsen, F.J.; Dam-Johansen, K.; Baxter, L.L. The implication of chlorine-associated corrosion on the operation of biomass-fired boilers. *Prog. Energy Combust. Sci.* **2000**, *26*, 283–298.
18. Dahneke, B. The capture of aerosol particles by surfaces. *J. Colloid Interface Sci.* **1971**, *37*, 342–353.
19. Dahneke, B. Measurements of the bouncing of small latex spheres. *J. Colloid Interface Sci.* **1973**, *45*, 584–590.
20. Dahneke, B. Further measurements of the bouncing of small latex spheres. *J. Colloid Interface Sci.* **1975**, *51*, 58–65.
21. Rogers, L.N.; Reed, J. The adhesion of particles undergoing an elastic-plastic impact with a surface. *J. Phys. D Appl. Phys.* **1984**, *17*, 677–689.
22. Wall, S.; John, W.; Wang, H.-C.; Goren, S.L. Measurements of kinetic energy loss for particles impacting surfaces. *Aerosol Sci. Technol.* **1990**, *12*, 926–946.
23. Dunn, P.F.; Brach, R.M.; Caylor, M.J. Experiments on the low-velocity impact of microspheres with planar surfaces. *Aerosol Sci. Technol.* **1995**, *23*, 80–95.
24. Van Beek, M.C.; Rindt, C.C.M.; Wijers, J.G.; van Steenhoven, A.A. Rebound characteristics for 50-μm particles impacting a powdery deposit. *Powder Technol.* **2006**, *165*, 53–64.

25. Kim, O.V.; Dunn, P.F. Direct visualization and model validation of microsphere impact and surface capture. *J. Aerosol Sci.* **2008**, *39*, 373–375.
26. Shuiqing, L.; Marshall, J.S.; Guanqing, L.; Qiang, Y. Adhesive particulate flow: The discrete-element method and its application. *Prog. Energy Combust. Sci.* **2011**, *37*, 633–668.
27. Brach, R.M.; Dunn, P.F. Macrodynamics of microparticles. *Aerosol Sci. Technol.* **1995**, *23*, 51–71.
28. Kim, O.V.; Dunn, P.F. A microsphere-surface impact model for implementation in computational fluid dynamics. *J. Aerosol Sci.* **2007**, *38*, 532–549.
29. Li, X.; Dunn, P.F.; Brach, R.M. Experimental and numerical studies on the normal impact of microspheres with surfaces. *J. Aerosol Sci.* **1999**, *30*, 439–449.
30. Matsunaga, T.; Kim, J.K.; Rohatgi, P.K. Crystallinity and selected properties of fly ash particles. *Mater. Sci. Eng. A* **2002**, *325*, 333–343.
31. Chung, F.H. Quantitative interpretation of X-ray diffraction patterns of mixtures. II. Adiabatic principle of X-ray diffraction analysis of mixtures. *J. Appl. Crystallogr.* **1974**, *7*, 526–531.
32. Shackelford, J.F.; Alexander, W. *The CRC Materials Science and Engineering Handbook*; CRC Press: Boca Raton, FL, USA, 1992; pp. 436–438.
33. Bitter, J.G.A. A study of erosion phenomena part I. *Wear* **1963**, *6*, 5–21.
34. Johnson, K.L.; Kendall, K.; Roberts, A.D. Surface energy and the contact of elastic solids. *Proc. R. Soc. Lond.* **1971**, *324*, 301–313.
35. Thomton, C.; Ning, Z. A theoretical model for the stick/bounce behaviour of adhesive, elastic-plastic spheres. *Powder Technol.* **1998**, *99*, 154–162.
36. Liu, G.; Li, S.; Yao, Q. A JKR-based dynamic model for the impact of micro-particle with a flat surface. *Powder Technol.* **2011**, *207*, 215–223.
37. Abd-Elhady, M.S.; Rindt, C.C.M.; Wijers, J.G.; van Steenhoven, A.A. Modeling the impaction of a micron particle with a powdery layer. *Powder Technol.* **2006**, *168*, 111–124.